

# ESTIMATION OF SLENDER BODY ELASTIC RATES AND ACCELERATIONS USING A COMBINATION OF MEASURED DATA

Ilya Genkin<sup>1</sup> and Daniella E. Raveh<sup>1</sup>

<sup>1</sup>Faculty of Aerospace Engineering  
Technion - Israel Institute of Technology, Haifa, 3200003, Israel  
ilyagen@campus.technion.ac.il, daniella@technion.ac.il

**Keywords:** Aeroelasticity, Kalman state estimator, sensor fusion, state-space, slender

**Abstract:** The paper presents a methodology to estimate the in-flight elastic and rigid-body dynamics of a slender flexible body using multiple data and an approximate aeroelastic model. It is intended to overcome the inherent shortcoming of flight control systems that typically rely on a rigid-body model whereas the measured response includes both the rigid-body dynamics and the elastic dynamic response. The study presents a Kalman state estimation approach based on an approximated aeroelastic model of the vehicle dynamics and a combination of measured data from different sensors, to estimate structural modal deformations, rates, and accelerations. The estimated states can then be used to reconstruct the elastic response at the IMU location, from which the rigid body dynamics can be computed. The paper presents the test case of a simple slender-body vehicle under random time-varying loading. Numerical results show that the proposed methodology accurately reconstructs the elastic dynamic elastic response. A parametric study presents the effect of using different sensor data of various noise levels.

## 1 INTRODUCTION

Flight control systems (FCS) of flight vehicles rely on data, specifically, angular rates and accelerations, commonly measured by a strap-down inertial measurement unit (IMU). These measurements capture and reflect both the rigid body motion of the vehicle, exhibited mainly in lower frequencies, and its elastic dynamic deformations, occurring in the relatively higher frequency range. The FCS, which aims to regulate a vehicle's trajectory, is typically designed based on a rigid-body dynamics model, while the elastic modes are unmodeled. For such a control system, the presence of accelerations and angular rates due to elastic vibrations in the measurement is undesirable and must be accounted for. For a flexible slender body, the elastic normal modes of the structure are in the lower frequencies, such that the elastic dynamic response might be in the bandwidth of the FCS [1]; thus, special care is needed to filter out the elastic response from the measurement, to avoid instabilities due to the FCS action.

The common practice in such systems is to remove the elastic motion component from the IMU data by applying a combination of low-pass and notch filters, filtering out the higher frequencies associated with the elastic motion, and retaining only the low-frequency data associated with the rigid body motion of the vehicle. This requires in-advance estimation of the elastic frequencies. However, the structural natural frequencies of slender vehicles, such as space launchers or missiles, significantly vary during a flight mission due to fuel consumption and stage separations, which change the inertial properties and geometry of the body. Moreover, the aerodynamic forces also introduce stiffness-like terms, changing the aeroelastic frequencies of the vehicle as a

function of flight conditions (e.g., altitude and Mach number). Therefore, the *a priori* estimation of the aeroelastic frequencies of the vehicle throughout its mission is challenging.

As it is impractical to create and calibrate in advance a structural model for every state and flight condition of the mission, the extreme frequencies, corresponding to the extreme flight conditions, are computed using numerical finite element (FE) models, or experimentally estimated in ground vibration tests (GVT) of representative states of the vehicle. Using the computed extreme frequencies, frequency bands are defined and inputted into the FCS [2]. Typically, the filtering is based solely on frequencies, disregarding the shape and amplitude of the elastic mode. Consequently, the notch filter attenuation exceeds the requirements, resulting in a broader filtered frequency band, reducing the stability margins of the FCS, and possibly even reducing the effective bandwidth of the driving actuators.

In today's platforms, measured data of the elastic accelerations and strains has become more accessible. Specifically, acceleration over the body can be measured by small accelerometers while multiple strain data can be captured with optical fibers. These offer accurate large data on the dynamic elastic motion. The current study explores how this data can be leveraged to estimate the rigid-body dynamics accurately. A recent study introduced a state estimation approach in which the elastic states were estimated using an aeroelastic model, dynamic strain data, and the Kalman state estimator (KSE) [3].

In the current study, we propose to utilize the KSE for assessing the dynamic structural modal deformations, rates, and accelerations based on an approximate aeroelastic state-space model of the vehicle and a combination of measured data, from integrated fiber-optics strain sensors (FOSS), and other sensors commonly installed over the vehicle, such as accelerometers and gyroscopes. The estimated states can then be used to reconstruct the elastic response at the inertial measurement units (IMU) location, such that it can be removed from the inertial measurements, from which the center of mass rigid-body dynamics can be computed.

The current study extends the KSE approach in that the modal accelerations are estimated directly from the data (rather than computed based on the estimated displacements and rates). This is possible due to the use of an approximated model, where the unknown dynamics of the model are modeled as process noise, and the use of a combination of measurements from different sensors, each dependent on a different state in the approximated model, making all the modal states observable.

The study presents the formulation of an aeroelastic state-space model, and analyzes a test case of a simple slender body vehicle under random time-varying forcing, commonly happening due to aerodynamic turbulence. The test case uses an approximate aeroelastic model that does not include the external excitation (considered as process noise). In the test case it is assumed that the structural properties of the vehicle, as well as the flight conditions are constant during some time window, representative of one phase of the flight mission. This assumption acts as yet another approximation, making the calculation of the response use assumed modes instead the real modes, with the participation factors adjusted by the KSE accordingly using the measurements of the sensors. The reference response is calculated from the full response to the excitation. The measured data is simulated as the response to the excitation at specific points defined as sensors, contaminated with noise. The test case demonstrates that the use of the KSE approach with an approximated model yields good estimation of the rigid body response of the vehicle.

## 2 MATHEMATICAL MODEL

### 2.1 Aeroelastic state-space formulation

The equations of motion of an aeroelastic system, in modal coordinates, are given as [4]

$$[M_{ae}]\{\ddot{\xi}\} + [C_{ae}]\{\dot{\xi}\} + [K_{ae}]\{\xi\} - q_\infty [D]\{X_a\} = \{F_{e_h}\} \quad (1)$$

where  $\{\xi\}$  is the modal displacement vector and  $\{X_a\}$  is the aerodynamic lag vector, defined in the Laplace domain as:

$$\{X_a\} = \left( s[I] - \frac{V}{L}[R] \right)^{-1} [E]s\{\xi\} \quad (2)$$

$[M_{ae}]$ ,  $[C_{ae}]$  and  $[K_{ae}]$  are the aeroelastic mass, damping, and stiffness generalized matrices, respectively, defined as (by using mass-normalized modes):

$$\begin{aligned} [M_{ae}] &= [I] - q_\infty \frac{L^2}{V^2} [A_2] \\ [C_{ae}] &= 2[Z][\Omega] - q_\infty \frac{L}{V} [A_1] \\ [K_{ae}] &= [\Omega]^2 - q_\infty [A_0] \end{aligned}$$

The matrices  $[A_0]$ ,  $[A_1]$  and  $[A_2]$  represent the aerodynamic stiffness, damping and apparent mass of the unsteady aerodynamics, respectively, and  $[R]$  is a diagonal matrix containing the aerodynamic lag roots that model the aerodynamic lag effects.  $[D]$  and  $[E]$  are coupling matrices between the lag terms and the modal displacements. [5]

To estimate the modal accelerations together with the modal displacements and velocities, vector  $\{\ddot{\xi}\}$  is added to the state vector by introducing an expression for its time derivative:

$$\{\ddot{\xi}\} = -[M_{ae}]^{-1}[K_{ae}]\{\xi\} - [M_{ae}]^{-1}[C_{ae}]\{\dot{\xi}\} + q_\infty [M_{ae}]^{-1}[D]\{\dot{X}_a\} + [M_{ae}]^{-1}\{\dot{F}_{e_h}\} \quad (3)$$

The aerodynamic-lag rate,  $\{\dot{X}_a\}$ , is also included as part of the state vector by introducing  $\{\ddot{X}_a\}$  based on the time derivation of equation (2):

$$\{\ddot{X}_a\} = [E]\{\ddot{\xi}\} + \frac{V}{L}[R]\{\dot{X}_a\} \quad (4)$$

The state vector,  $\{x\}$ , is defined as:

$$\{x\} = \begin{Bmatrix} \xi \\ \dot{\xi} \\ \ddot{\xi} \\ X_a \\ \dot{X}_a \end{Bmatrix} \quad (5)$$

and the input vector  $\{u\}$  is defined as:

$$\{u\} = \{\dot{F}_{e_h}\} \quad (6)$$

The resulting state equation is:

$$\{\dot{x}\} = \begin{bmatrix} 0 & [I] & 0 & 0 & 0 \\ 0 & 0 & [I] & 0 & 0 \\ 0 & -[M_{ae}]^{-1}[K_{ae}] & -[M_{ae}]^{-1}[C_{ae}] & 0 & q_{\infty}[M_{ae}]^{-1}[D] \\ 0 & 0 & 0 & 0 & [I] \\ 0 & 0 & [E] & 0 & \frac{V}{L}[R] \end{bmatrix} \{x\} + \begin{bmatrix} 0 \\ 0 \\ [M_{ae}]^{-1} \\ 0 \\ 0 \end{bmatrix} \{u\} \quad (7)$$

Using the modal method, each physical response can be reconstructed as a linear combination of a set of normal modes as:

$$\begin{Bmatrix} \epsilon \\ w \\ \dot{w} \\ \ddot{w} \\ \theta \\ \dot{\theta} \end{Bmatrix} = \begin{bmatrix} [\Psi] & 0 & 0 & 0 & 0 \\ [\Phi] & 0 & 0 & 0 & 0 \\ 0 & [\Phi] & 0 & 0 & 0 \\ 0 & 0 & [\Phi] & 0 & 0 \\ [\Phi_r] & 0 & 0 & 0 & 0 \\ 0 & [\Phi_r] & 0 & 0 & 0 \end{bmatrix} \begin{Bmatrix} \xi \\ \zeta \\ \dot{\xi} \\ \dot{\zeta} \\ X_a \\ \dot{X}_a \end{Bmatrix} \quad (8)$$

where  $\epsilon$ ,  $w$ ,  $\dot{w}$  and  $\ddot{w}$  are the strain and physical displacements, velocities and accelerations at some nodes and  $\theta$  and  $\dot{\theta}$  are the physical rotations and angular velocities.  $[\Phi]$  and  $[\Psi]$  are the displacement and strain modes matrices, and  $[\Phi_r]$  is the rotation modes matrix, all provided at the physical nodes where the responses are recovered. By utilizing the state vector as defined in equation (5), physical responses can be reconstructed directly, without requiring the input  $\{u\}$ . This is advantageous because, in this formulation, the input is the time variation of the generalized external forces, which is unknown.

The normal modes matrices in equation (8) could be reduced matrices, holding only the rows corresponding to the required output points, such as the location of the IMU in the vehicle, or the locations of the sensors spread throughout the vehicle. The augmented aerodynamic states  $X_a$  and  $\dot{X}_a$  are not used for the reconstruction of the physical parameters, but are needed as part of the state's computation. It is evident from equation (8) that an informed choice of a combination of commonly available sensors, such as FOSS, gyroscopes and accelerometers, can yield a measurement equation in which all the modal states are observable.

The state-space representation of the IMUs of the vehicle, which measures the acceleration and the angular rate of the vehicle, is therefore:

$$\{\dot{x}\} = \begin{bmatrix} 0 & [I] & 0 & 0 & 0 \\ 0 & 0 & [I] & 0 & 0 \\ 0 & -[M_{ae}]^{-1}[K_{ae}] & -[M_{ae}]^{-1}[C_{ae}] & 0 & q_{\infty}[M_{ae}]^{-1}[D] \\ 0 & 0 & 0 & 0 & [I] \\ 0 & 0 & [E] & 0 & \frac{V}{L}[R] \end{bmatrix} \{x\} + \begin{bmatrix} 0 \\ 0 \\ [M_{ae}]^{-1} \\ 0 \\ 0 \end{bmatrix} \{u\}$$

$$\{y\}_{IMU} = \begin{bmatrix} 0 & 0 & [\Phi_{IMU}] & 0 & 0 \\ 0 & [\Phi_{rIMU}] & 0 & 0 & 0 \end{bmatrix} \{x\} \quad (9)$$

where  $[\Phi_{IMU}]$  and  $[\Phi_{rIMU}]$  are the displacement and rotation modes matrices, respectively, represented at the locations of the IMUs in the vehicle.

## 2.2 Approximated state-space model

The approximated model assumes no external excitation forces. If a time-varying external load is present, it is considered, along with other unmodeled dynamics, as process noise. Additionally, in general, the state-space model may change in time, since both the structural properties and the flight conditions vary during flight. In this study, we consider both structural properties and flight conditions invariant within a time window during the flight. Thus, the time variation of the state-space model is considered an additional approximation.

The state-space formulation of equation (7), considering model approximations, uncertainties and measurement noise, becomes:

$$\begin{aligned}\{\dot{x}\} &= [A]\{x\} + \{w\} \\ \{y\} &= [C]\{x\} + \{v\}\end{aligned}\quad (10)$$

where  $\{w\} \sim \mathcal{N}(0, Q)$  and  $\{v\} \sim \mathcal{N}(0, R)$  are uncorrelated zero-mean normally distributed process and measurement noise with covariance matrices  $Q$  and  $R$ , respectively,  $[A]$  is the state transition matrix:

$$[A] = \begin{bmatrix} 0 & [I] & 0 & 0 & 0 \\ 0 & 0 & [I] & 0 & 0 \\ 0 & -[M_{ae}]^{-1}[K_{ae}] & -[M_{ae}]^{-1}[C_{ae}] & 0 & q_{\infty}[M_{ae}]^{-1}[D] \\ 0 & 0 & 0 & 0 & [I] \\ 0 & 0 & [E] & 0 & \frac{V}{L}[R] \end{bmatrix}\quad (11)$$

and  $[C]$  is the state output matrix defined based on the required outputs. This state-space formulation essentially solves the free vibration problem of the aeroelastic system, driven by process noise.

## 2.3 Kalman state estimator (KSE)

The KSE uses a system's dynamic model, known control inputs to the system, and multiple sequential measurements to estimate the system's states. At each time step, the state estimation is based on a weighted average of the model's prediction and the new measurement set, with the larger weight given to the component of greater certainty [6]. The algorithm optimally minimizes the covariance of uncertainties, effectively handling noisy sensor data and process uncertainty. The algorithm operates recursively and requires only the latest system state estimate to calculate a new state, making it suitable for real-time control during flight.

Since the measurements are sampled in discrete times, a discrete state-space model is formulated based on equation (10), as:

$$\begin{aligned}\{x_{k+1}\} &= [F]\{x_k\} + \{w_k\} \\ \{z_k\} &= [H]\{x_k\} + \{v_k\}\end{aligned}\quad (12)$$

where  $[F]$  is the discrete state transition matrix, calculated from the continuous state-space transition matrix  $[A]$  as:

$$[F] = e^{[A]\Delta t}\quad (13)$$

where  $\Delta t$  is the sampling time of the discrete system.

The measurement vector  $\{z_k\}$  contains a combination of data from strain, angular rate, and acceleration sensors. The observation matrix  $[H]$  is constructed using the modal method, where

the corresponding modes are provided at the sensor points:

$$\{z_k\} = \begin{Bmatrix} \epsilon_s \\ \dot{w}_s \\ \dot{\theta}_s \end{Bmatrix}_k = \begin{bmatrix} [\Psi_s] & 0 & 0 & 0 & 0 \\ 0 & 0 & [\Phi_s] & 0 & 0 \\ 0 & [\Phi_{r_s}] & 0 & 0 & 0 \end{bmatrix} \begin{Bmatrix} \xi \\ \dot{\xi} \\ \ddot{\xi} \\ X_a \\ \dot{X}_a \end{Bmatrix}_k = [H]\{x_k\} \quad (14)$$

The state-space matrices are assumed constant within the considered time window, and as such, both the state transition matrix  $[F]$  and the observation matrix  $[H]$ , as well as the covariance matrices  $[Q]$  and  $[R]$ , are also constant during the considered time window.

For the discrete state-space model (equation (12)), a discrete KSE is defined using a two-step prediction-correction formulation as follows:

Prediction Step:

$$\text{State Estimate:} \quad \{\hat{x}_{k+1|k}\} = [F]\{\hat{x}_{k|k}\} \quad (15)$$

$$\text{Error Covariance:} \quad [P_{k+1|k}] = [F][P_{k|k}][F]^T + [Q] \quad (16)$$

Correction Step:

$$\text{Kalman Gain:} \quad [K_{k+1}] = [P_{k+1|k}][H]^T([H][P_{k+1|k}][H]^T + [R])^{-1} \quad (17)$$

$$\text{State Estimate:} \quad \{\hat{x}_{k+1}\} = \{\hat{x}_{k+1|k}\} + [K_{k+1}](\{z_k\} - [H]\{\hat{x}_{k+1|k}\}) \quad (18)$$

$$\text{Error Covariance:} \quad [P_{k+1}] = ([I] - [K_{k+1}][H])[P_{k+1|k}] \quad (19)$$

where  $\{\hat{x}\}$  is the estimated state,  $[P]$  is the state estimation error covariance defined as  $[P] = \mathbb{E}[(x - \hat{x})^2]$  and  $[K]$  is the Kalman gain matrix. The double index notation,  $a|b$ , stands for the value calculated at time index  $a$ , based on the known value at time index  $b$ , and is used to add an intermediate time index between the prediction and correction steps.

At each time step, the state vector is estimated by the KSE and then used to calculate the estimated elastic response of the IMU:

$$\{\hat{y}_k\}_{IMU} = \begin{bmatrix} 0 & 0 & [\Phi_{IMU}] & 0 & 0 \\ 0 & [\Phi_{r_{IMU}}] & 0 & 0 & 0 \end{bmatrix} \{\hat{x}_k\} \quad (20)$$

The estimated vehicle's rigid body response,  $\hat{y}_R$ , can be extracted by subtracting the estimated elastic response from the overall measurement of the IMU:

$$\{\hat{y}_R\}_{IMU} = \{y\}_{IMU} - \{\hat{y}\}_{IMU} \quad (21)$$

### 3 TEST CASE

The proposed method is tested using a simplified missile model of 6 m length and 0.2 m diameter. The model is composed of 3 parts representing the mechanical properties of an outer structure, a solid propellant, and a payload. A structural FE model and an aerodynamic panel model were created to formulate the aeroelastic and KSE models. These models are presented in the following subsections.

### 3.1 Structural finite element model

A FE model was built using MSC Patran commercial software. The primary structure was modeled using shell elements, each with a constant thickness of 4 mm and standard material properties of Aluminum ( $E = 71 \text{ GPa}$ ,  $\nu = 0.33$ ,  $\rho = 2810 \text{ kg/m}^3$ ). The solid propellant section was modeled using 1D bar elements of a ring-shaped cross-section with an inner diameter of 0.02 m and an outer diameter equal to the model's diameter, of 0.2 m. Material properties are typical of standard solid rocket motor propellant ( $E = 5 \text{ MPa}$ ,  $\nu = 0.25$ ,  $\rho = 2000 \text{ kg/m}^3$ ). Each node of the propellant bar elements was rigidly connected to the outer structure's cross-section. The payload was modeled as a lumped mass (0D point element), weighting 60 kg also connected rigidly to the outer structure at the same cross-section. Figure 1 shows the FE model. For simplicity, the analysis of the symmetric model was performed in the X-Y plane only.

To simulate sensor measurements, sensor points were defined along the model's top ( $Y = R$ ) directrix. The sensor points are marked with red squares in figure 1. For simplicity, any sensor point can represent either a strain, acceleration, or angular rate measurement, or any combination of them. For a strain measurement, it was assumed that the measurements come from a fiber-optic strain sensor installed on the outer side of the structure along the axial direction, considering only the  $\epsilon_{xx}$ . For the acceleration measurement, the Y-direction accelerations,  $\ddot{w}$ , were considered, and for the angular rates, the rotation rates around the Z axis  $\dot{\theta}$  were considered. The acceleration and angular rate sensors were assumed to be installed above or below the propellant, as sensors are typically not installed in the solid rocket motor structure. The IMU was positioned in the front part of the missile, indicated by a green square in figure 1.

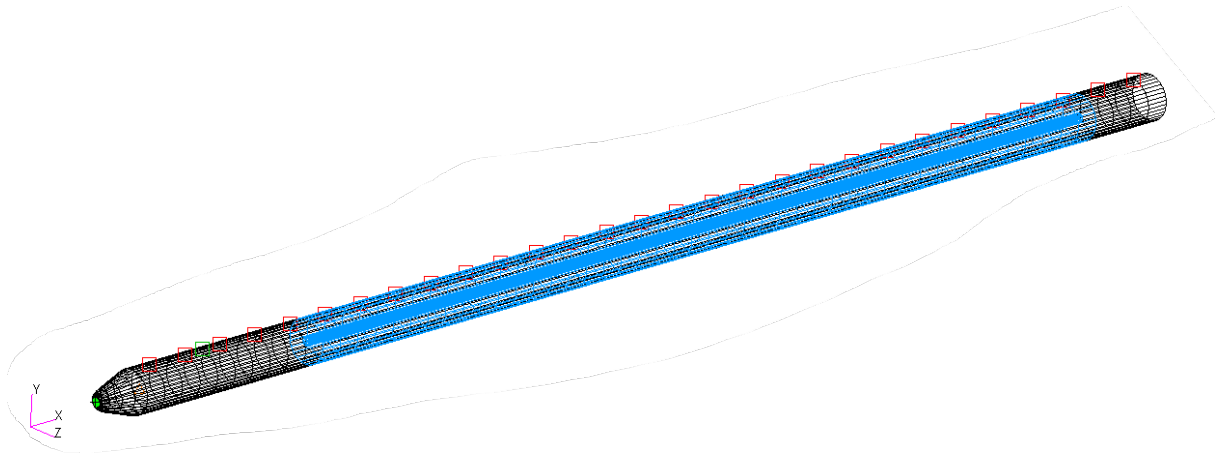


Figure 1: Test case finite elements model. Sensor points are marked with red squares. IMU output point is marked with a green square.

Free vibration analysis of the free-free model was performed using commercial FE solver MSC Nastran SOL 103 to determine the natural frequencies of the model and construct all the normal modes matrices required for the state-space representation. The results are summarized in table 1. For the estimation in the test case, only the first three elastic bending modes were used, as the following modes are excited at higher frequencies and are not expected to contribute significantly to the system's response. Figure 2 depicts the displacement, rotation, and strain components of the first three elastic bending modes, at the sensors' locations.

Mode shape	Frequency [Hz]	Generalized Stiffness ( $\omega_n^2$ ) [Nm]	Generalized Mass [kgm <sup>2</sup> ]
Surge	0	0	1.0
Pitch	0	0	1.0
Heave	0	0	1.0
1 <sup>st</sup> Bending	12.6	6.335e3	1.0
2 <sup>nd</sup> Bending	35.7	5.041e4	1.0
3 <sup>rd</sup> Bending	72.7	2.087e5	1.0
4 <sup>th</sup> Bending	122.2	5.899e5	1.0
1 <sup>st</sup> Tensile	152.9	9.227e5	1.0
5 <sup>th</sup> Bending	181.6	1.303e6	1.0
6 <sup>th</sup> Bending	248.0	2.428e6	1.0

Table 1: Summary of the structural modal properties of the first calculated 10 normal modes of the test case FE model.

### 3.2 Aerodynamic panels model

For the construction of the aeroelastic state-space model, matrices  $[A_0]$ ,  $[A_1]$ ,  $[A_2]$ ,  $[D]$ , and  $[E]$  were calculated using RFA with the ZAERO commercial aeroelastic software, utilizing the aeroservoelasticity module of the solver.

The matrix  $[Q_{hh}]$  can be divided into terms corresponding to rigid body modes and elastic modes as:

$$[Q_{hh}] = \begin{bmatrix} Q_{rr} & Q_{re} \\ Q_{er} & Q_{ee} \end{bmatrix} \quad (22)$$

where subscript  $r$  refers to rigid body modes and  $e$  refers to elastic modes. The calculation and RFA of matrix  $[Q_{hh}]$  are performed for all terms. However, as only the elastic response is considered, only the terms of  $[Q_{ee}]$  are utilized to construct the KSE transition matrix. Aeroelastic coupling between the rigid body and elastic dynamics is neglected as it is considered of second order.

ZAERO utilizes the aerodynamic panel method to compute the AIC matrix via different methods for various flight conditions. For the current test case, a supersonic airspeed of Mach=2.0 was selected, with sea-level atmospheric conditions. The aerodynamic panel model is composed of a single body mesh segment, divided into 65 sections along the longitudinal axis. The nose is defined as an inlet aerodynamic box with 0% flow penetrating the body (this is because at supersonic velocities it is considered a superinclined box [5]). The aerodynamic model was related to the structural model using the thin-plane spline module.

A sensitivity analysis for various approximation parameters was conducted, comparing Roger's [7] and the Minimum State (MS) [8] methods, and using a different number of aerodynamic lag terms. Figure 3 shows a comparison of  $[Q_{hh}]$  terms as computed by the RFAs and directly by the aerodynamic model in the frequency domain for a range of reduced frequencies  $0.005 < k < 2.5$ . Based on the sensitivity analysis, the state-space model was built with RFA using Roger's method with three aerodynamic lag terms.

### 3.3 Random time-varying excitation force

Missile vehicles are subjected to aerodynamic pressure excitation from different sources including shockwaves, turbulent boundary layers (TBL), and recirculating flows, which have broad-

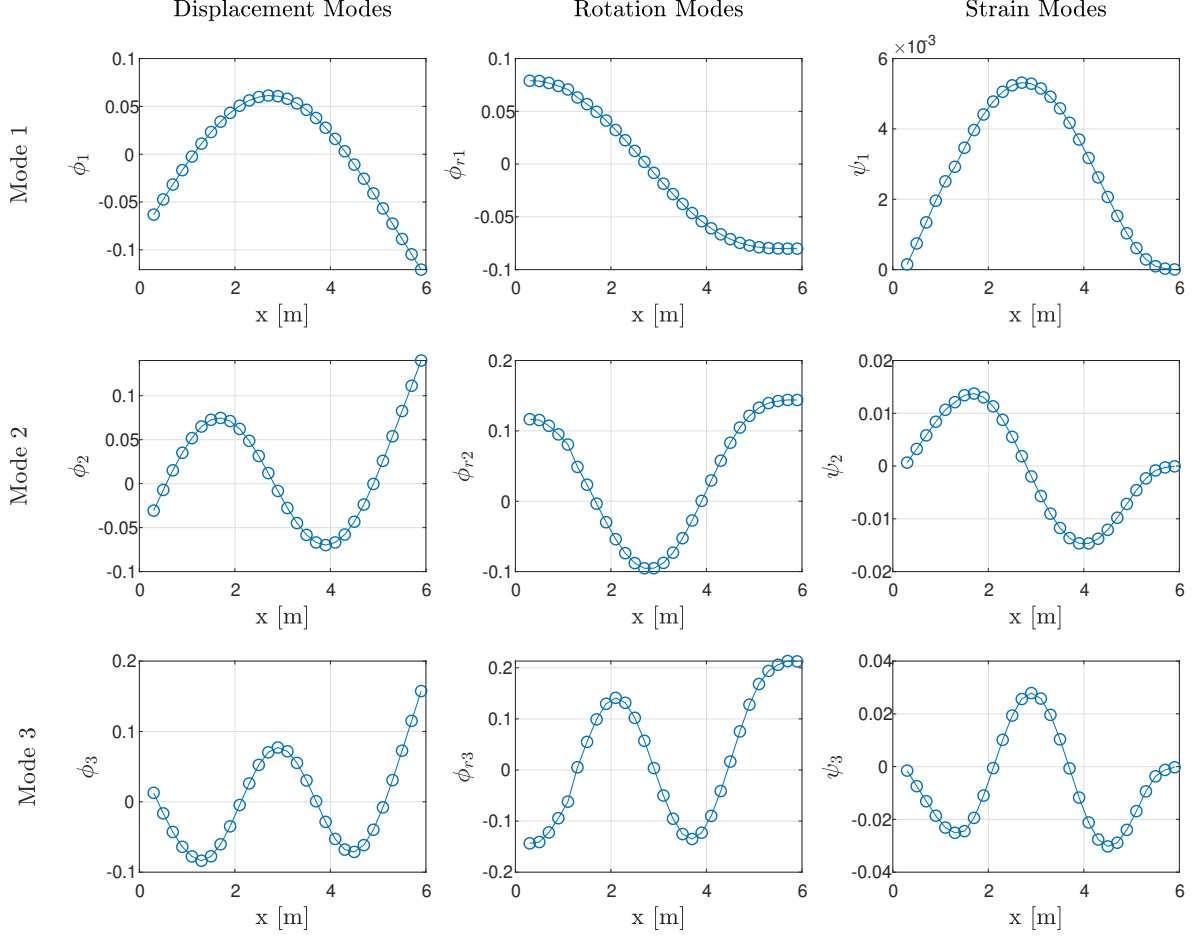


Figure 2: Displacement, rotation, and strain elements of the first three elastic bending modes of the test case model.

band random characteristics. The aerodynamic excitation is most severe during the vehicle's maximum dynamic pressure flight phase.

Different empirical methods exist for determining the aerodynamic pressure power spectral density (PSD) along a missile's body derived for various flow regimes using measurements of various missiles [9]. A simplified excitation based on the attached flow over a cone-cylinder structure for supersonic velocities was used for the current test case. The pressure PSD in the turbulent boundary layer of the attached flow is expressed as:

$$G(x, \bar{\omega}) = \frac{4P_{rms}^2 \delta^*(x)}{V} \left[ \frac{F^{1.433}}{1 + (F^{1.433} \bar{\omega})^2} \right] \quad (23)$$

where  $F$  is some empirical constant depending on the Mach number and is taken as  $F = 1 + 0.13M^2$ ,  $P_{rms}$  is the Root-Mean-Square (RMS) pressure value of the attached flow and is calculated as  $P_{rms} = q_\infty \frac{0.01}{F}$ , where  $q_\infty = \frac{1}{2} \rho V^2$  is the dynamic pressure with  $V$  being the flight velocity,  $\bar{\omega}$  is a normalized frequency defined as  $\bar{\omega} = \frac{\omega \delta^*}{V}$ .  $\delta^*$  is the displacement thickness of the TBL and is defined as:

$$\delta^*(x) = 0.0371x(Re)^{-0.2} \left[ \frac{\frac{9}{7} + 0.475M^2}{(1 + 0.13M^2)^{0.64}} \right] \quad (24)$$

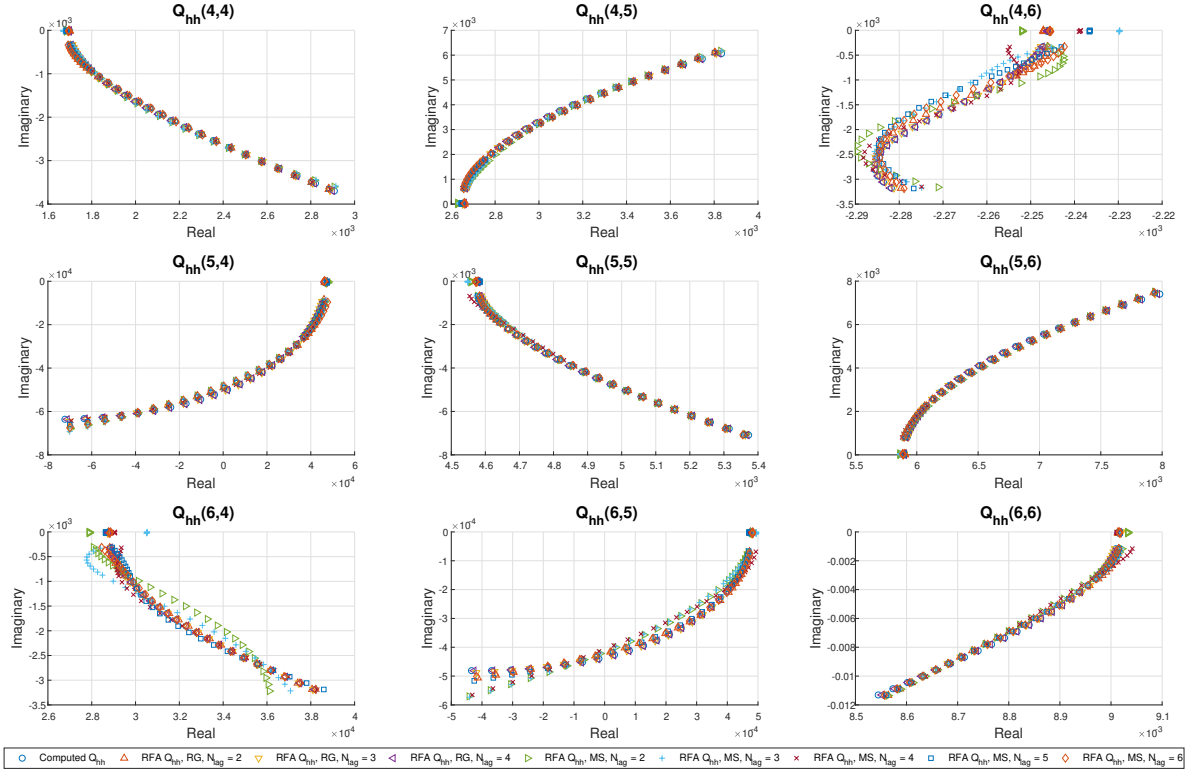


Figure 3: Comparison of approximated and computed  $[Q_{hh}]$  matrix terms for different numbers of aerodynamic lag terms, using either Roger's or Minimum State method, for the case study model having  $N_h = 6$ , where first 3 modes are rigid body and modes 4-6 are elastic. Only terms of  $[Q_{ee}]$  are shown.

With  $Re$  the Reynolds number and  $M$  the Mach number.

The pressure excitation acts normal to the surface of the structure and is different along the axial stations of the vehicle, both in amplitude and in spectral shape, since both the amplitude of the PSD and the normalized frequency are functions of the displacement thickness ( $\delta^*$ ) of the TBL. To simplify the calculation for the test case, the excitation was assumed as broadband random excitation with constant spectral density (white noise) at all the stations along the structure, having the same RMS amplitude of the shaped spectral density. The RMS value of the shaped PSD is:

$$G_{rms}(x) = \sqrt{\int_0^\infty G(x, \bar{\omega}) d\bar{\omega}} = P_{rms} \sqrt{\frac{2\pi\delta^*(x)}{V}} \quad (25)$$

Therefore, the external aerodynamic force exciting the structure is a random force with normal distribution having zero-mean and variance of  $G_{rms}^2(x)$ , that is  $\{F_e\} \sim \mathcal{N}(0, G_{rms}^2(x))$ , which results in different amplitudes along the model's longitudinal axis. Since the analysis is performed in the X-Y plane only, and the pressure forces act normal to the structure's surface, only the forces acting on the  $y = \pm R$  edges of the structure were modeled. Figure 4 shows a representation of the forces exciting the system for the case study model, the size of the arrows is proportional to the RMS value calculated at each station of the model.

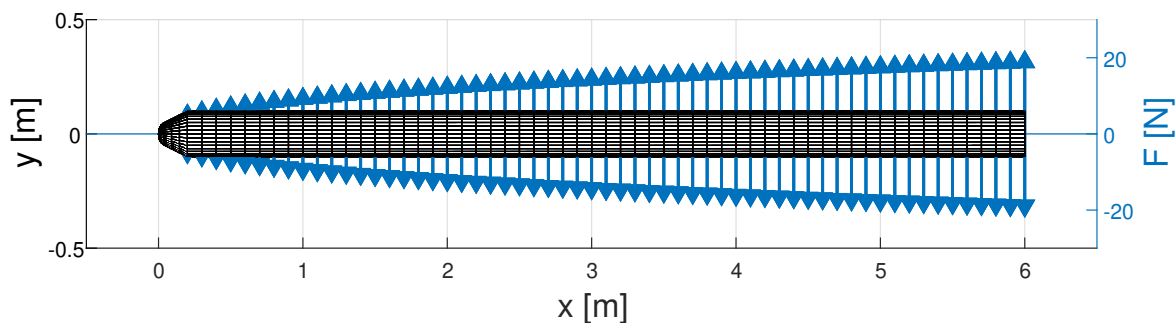


Figure 4: Aerodynamic forces acting along the model. The force values represent the forces' RMS amplitudes.

### 3.4 KSE implementation

To implement the KSE, the uncertainty matrices  $[Q]$  and  $[R]$  are required, along with an initial state vector  $\{x_0\}$  and the initial estimation error covariance matrix  $[P_{0,0}]$ . The optimal tuning of the KSE parameters is not within the scope of the current study; hence, all values are derived from assumptions or bounding values.

#### 3.4.1 Measurement noise covariance

The measurement noise originates from the sensor noise. All sensors are modeled as uncorrelated, with zero-mean Gaussian noise defined by the variance corresponding to the type of sensor. A baseline level of noise covariance was established using typical commercial sensors data. The covariance values chosen were:  $\sigma_\epsilon^2 = 5 \mu\text{s}^2$  for FOSS,  $\sigma_{\dot{w}}^2 = 1\text{e-}3 \frac{\text{m}^2}{\text{s}^4}$  for the accelerometer, and  $\sigma_{\dot{\theta}}^2 = 5\text{e-}4 \frac{\text{rad}^2}{\text{s}^2}$  for the gyroscope. With  $N_\epsilon$  strain sensor measurement points,  $N_{\dot{w}}$  acceleration measurement points, and  $N_{\dot{\theta}}$  angular velocity measurement points, the resulting  $[R]$  matrix is:

$$[R] = \begin{bmatrix} \sigma_\epsilon^2 [I]_{N_\epsilon \times N_\epsilon} & & \\ & \sigma_{\dot{w}}^2 [I]_{N_{\dot{w}} \times N_{\dot{w}}} & \\ & & \sigma_{\dot{\theta}}^2 [I]_{N_{\dot{\theta}} \times N_{\dot{\theta}}} \end{bmatrix} \quad (26)$$

such that the overall size of matrix  $[R]$  is  $N_\epsilon + N_{\dot{w}} + N_{\dot{\theta}} \times N_\epsilon + N_{\dot{w}} + N_{\dot{\theta}}$ , depending on the number of each sensor type used.

#### 3.4.2 Process noise covariance

The process noise corresponds to model inaccuracies (such as different stiffness due to simplification during FE modeling of the structure), model approximations (such as addressing the mass of the vehicle, or the dynamic pressure as constant during the calculated time window), and unmodeled dynamics of the system (not modeling the excitation force as part of the approximation, or having other unknown forces such as gust acting on the vehicle).

In this work, we will not estimate the model uncertainty but use bounding values to define the process noise. For the modal responses of the structure, we will base the bounding uncertainty using the maximal response of the structural system. Using the modal method for the elastic system, the system equation of motion results in an uncoupled system of equations, such that for each modal response, the equation has the form:

$$\ddot{\xi}_i + 2\omega_{n_i}\zeta_i\dot{\xi}_i + \omega_{n_i}^2\xi_i = \bar{f}_i \quad (27)$$

where  $\bar{f}_i$  is the generalized force acting on the  $i$ -th generalized coordinate. From the definition of the generalized force, the maximal force amplitude can be bounded as:

$$|f| = \left| \sum_{j=1}^N \phi_{ij}^T F_j \right| \leq \sum_{j=1}^N |\phi_{ij}^T| |F_j| \leq \sum_{j=1}^N |\phi_{ij}^T| F_{max} = F_{max} \sum_{j=1}^N |\phi_{ij}^T| = \|\phi_i^T\|_1 F_{max}$$

such that the generalized force can be bounded using the corresponding displacement mode shape and the maximal physical force amplitude expected to act on the system. The maximal generalized force is therefore defined as the bound:

$$|f|_{max} = \|\phi_i^T\|_1 F_{max} \quad (28)$$

The steady-state maximal modal displacement response is the response of the modal system to the maximal excitation force:

$$|\xi_i|_{max} = \frac{Q_i |f_i|_{max}}{\omega_{n_i}^2} \quad (29)$$

where  $Q_i$  is the Q factor, which is the maximal dynamic amplification of the response. Using equation (28) with the approximation of  $Q_i \approx \frac{1}{2\zeta}$  for low damping ratios, equation (29) becomes:

$$|\xi_i|_{max} = \frac{\|\phi_i^T\|_1 F_{max}}{2\zeta_i \omega_{n_i}^2} \quad (30)$$

Rewriting equation (30) in matrix form we get:

$$\{|\xi|\}_{max} = \frac{1}{2} [\Omega]^{-2} [Z]^{-1} \{\Phi_{norm}\} F_{max} \quad (31)$$

where  $\{\Phi_{norm}\} = \{\|\phi_1^T\|_1 \dots \|\phi_N^T\|_1\}^T$ . Similarly, expressions for the maximal modal velocity and acceleration responses can be derived as:

$$\{|\dot{\xi}|\}_{max} = \frac{1}{2} [\Omega]^{-1} [Z]^{-1} \{\Phi_{norm}\} F_{max} \quad (32)$$

$$\{|\ddot{\xi}|\}_{max} = \frac{1}{2} [Z]^{-1} \{\Phi_{norm}\} F_{max} \quad (33)$$

For the aerodynamic lag terms, using the definition of the lag states given in equation (2), since the  $[R]$  matrix is diagonal, the matrix term

$$\left( s[I] - \frac{V}{L} [R] \right)^{-1} s$$

is also a diagonal matrix having on its diagonal terms of the form  $\frac{s}{s+\beta_i}$ , where  $\beta_i$  is the  $i^{\text{th}}$  lag root. The amplitude of each such term is bounded by 1, such that the matrix term is bounded by the identity matrix  $[I]$ :

$$\left( s[I] - \frac{V}{L} [R] \right)^{-1} s \leq [I]$$

Therefore the maximal lag state amplitude is:

$$\{X_a\}_{max} \leq [E] \{|\xi|\}_{max} = \frac{1}{2} [E] [\Omega]^{-2} [Z]^{-1} \{\Phi_{norm}\} F_{max} \quad (34)$$

Similarly, expressions for the maximal lag state derivative amplitude can be derived as:

$$\{|\dot{X}_a|\}_{max} = \frac{1}{2}[E][\Omega]^{-1}[Z]^{-1}\{\Phi_{norm}\}F_{max} \quad (35)$$

The maximal force is taken as the maximal predicted force acting on the vehicle (figure 4). The process noise for the modal responses is taken as 10% of the maximal modal response. This value is arbitrary at this point, but its effect is investigated as part of the test case.

The resulting process noise vector is:

$$\{w\} = 0.1 \{|\xi|_{max} \quad |\dot{\xi}|_{max} \quad |\ddot{\xi}|_{max} \quad |X_a|_{max} \quad |\dot{X}_a|_{max}\}^T \quad (36)$$

The corresponding process covariance matrix is:

$$[Q] = \mathbb{E} [\{w\}\{w\}^T] \quad (37)$$

### 3.4.3 Q/R Factor

The Kalman gain defines for the KSE what to rely on, when assigning the weights between the model prediction and the measurements in each calculation step, based on the uncertainties of the process and the measurement. Looking at equation (17) we see that the gain depends on the ratio between the terms in the state estimate error covariance  $[P]$  and the measurement covariance matrix  $[R]$ . Substituting the expression for the state estimate error covariance (16), and neglecting the term for the state error covariance transition, as it should tend to minimum as the KSE converges, we get the Kalman gain to be:

$$[K] = [Q][H]^T ([H][Q][H]^T + [R])^{-1} \quad (38)$$

The observation matrix  $[H]$  is used to transform the process uncertainty matrix to the measurement space such that the terms of  $[H][Q][H]^T$  and  $[R]$  are comparable. We will denote:

$$[Q_R] = [H][Q][H]^T \quad (39)$$

Rearranging equation (18) we get:

$$\{\hat{x}_{k+1}\} = ([I] - [K_{k+1}][H]) \{\hat{x}_{k+1|k}\} + [K_{k+1}]\{z_k\} \quad (40)$$

When the the terms of  $[Q]$  are larger than those of  $[R]$ , meaning that the process uncertainty is larger than the measurement uncertainty, the Kalman gains will tend more to unity and the state estimate will be corrected mostly based on the measurements. In the opposite case, the Kalman gains will be low such that the state estimate will be corrected mostly based on the prediction of the state by the model.

Therefore, some metric should be defined to express the dominance of the interaction between the different uncertainties, denoted as Q/R ratio factor. Since the  $[R]$  matrix is diagonal, the factor is defined as the mean value of the ratio between the terms on the diagonals of  $[Q_R]$  and  $[R]$ :

$$f_{Q/R} = \frac{1}{N_s} \sum_{i=1}^{N_s} \frac{Q_{Rii}}{R_{ii}} \quad (41)$$

where  $N_s = N_\epsilon + N_{\ddot{w}} + N_{\dot{\theta}}$  is the total number of sensors. High values of  $f_{Q/R}$  should lead to an estimation that relies more on the measurements, and lower values of  $f_{Q/R}$  should lead to an estimation that relies more on the predictions using the state-space model.

### 3.4.4 Kalman state estimation initialization

To execute the estimation, initial conditions for the estimated state  $\{x_0\}$  and the state estimation error covariance  $[P_{0|0}]$  are needed. The system was assumed to be at rest, such that the state vector initial condition was taken as:

$$\{x_0\} = \{0\} \quad (42)$$

For the estimation error covariance, the  $[Q]$  matrix was used, such that:

$$[P_{0|0}] = [Q] \quad (43)$$

## 4 RESULTS

The first part of the results section provides the results of the test case simulation using the full aeroelastic state-space formulation, establishing the reference for the estimation. The following part presents the results of a parametric study concerning the effect of various sensor configurations on the estimation employing the approximated model and the proposed KSE approach. The last section of the results assumes the best sensor combination is selected, and presents an additional parametric study on the effect of the sensor noise levels and the process noise on the estimation.

### 4.1 Nominal response of the IMU

To investigate how the proposed KSE approach estimates the elastic response at the required IMU location, and extracts its rigid body response, an analysis of the IMU's nominal response is required. To compute the nominal response, the full state-space model described in section 2.1 was solved using the matrices derived from the mathematical models detailed in sections 3.1 and 3.2, for the random excitation input specified in section 3.3.

In general, for a time-varying aeroelastic model, the modal responses themselves are not of great interest, since the modal basis changes in time. The KSE, which calculates the response using an assumed constant modal basis, should compensate for the change in the modal bases by varying modal responses. In such cases, only the physical response may be used for evaluating the accuracy of the estimation. However, for a constant model, in which the structural properties and the flight conditions do not change, the modal basis is also constant, the physical responses are directly proportional to the modal responses, and the latter can be used to evaluate the estimation's accuracy.

The current test case considers a flight phase in which the structure and the flight conditions do not vary significantly. The approximate model is constructed using a fixed modal basis, and therefore the KSE estimated modal responses are expected to be similar to the full model's responses. Therefore, the KSE's performance will be evaluated based on both the modal and the physical responses.

### 4.2 Effect of sensor configuration

In the measurement equation formulation (14), each type of sensor measurement is directly proportional to one of the modal responses. However, each measurement location has a different sensitivity to each mode shape. The selection of a sensor placement has to consider the modes it observes, as well as the practical aspects of sensor installation. In this section, the selection of sensor configuration is explored. The number of sensors and their locations are selected such that all three elastic modes are observable, while still being feasible for real-world deployment.

For the strain sensors, since this study relies on FOSS, it was assumed that it is feasible to install a fiber as part of the rocket engine structure, such that axial strain data along the missile is available. Therefore, for the strain measurement, all measurement points were used, making all three elastic strain modes observable.

For the acceleration sensors, common accelerometers are installed on the internal part of the structure either ahead of the motor (measurement points 1-5 in figure 1) or behind it (measurement points 28-29 in figure 1). The acceleration reconstruction uses the displacement modes, which, in the case of a free-free slender body, obtain their maximum displacement at the free ends. However, because the center of mass of a free-free body is fixed in the elastic modes, for a structure with a non-uniform mass along the structure, the bending modes will also have a non-uniform displacement along the structure. Therefore, as can be seen from figure 2, the front end of the structure is not the optimal location for an accelerometer to observe the second and third modes.

For the angular rate sensors, measured by gyros, the installation strategy is similar to that of the accelerometers: They are located where the corresponding modes are most observable. The modes used for the angular rate reconstruction are the rotation modes. Since the rotation angle along the main axis is the axial derivative of the displacement, the rotation modes are zero where the displacement modes are maximal, and vice versa, except for the structure's edges. Therefore, the locations best suitable for displacement modes observability are the least suitable for rotation modes observability. In many real-life scenarios, however, a 6-DOF sensor that combines accelerations and angular rates is utilized, requiring a position selection that works well for both accelerometers and gyroscopes.

In the current study, both accelerometers and gyros were placed in measurement points 2, 5, and 28, where the displacement and rotation modes are not maximal, but are both observable and differentiable between each other. Figure 5 shows the locations of each sensor type.

Figure 6 shows the estimation of the modal responses using the KSE method for different combinations of sensor types. A close-up on a 0.1 sec representative section of the response is shown, such that the difference between different sensor combinations can be observed. The modal displacement is observed by the FOSS and therefore is accurately estimated in all cases since all cases have FOSS in the sensor configuration. The modal velocity is observed by the gyros, and therefore is best estimated in cases where there are angular rate measurements. However, for both the case of FOSS only, or FOSS and accelerometers, the modal velocities estimation is also adequate. The modal acceleration is observed by the accelerometers and therefore is best estimated in cases where there are acceleration measurements. The modal acceleration exhibits the largest elastic response to the dynamic generalized force excitation, and therefore, an accurate estimate is obtained only in cases where there are acceleration measurements.

Figure 7 shows the extracted rigid body response at the IMU location using the KSE with different sensor configurations. Similarly to the modal responses, figure 7 shows that in all cases an adequate extraction is achieved. However, the best estimations of the IMU's rigid-body accelerations or angular rates are achieved in cases where there are acceleration or angular rates measurements, respectively.

Figure 8 shows the PSD of the rigid body response at the IMU location (the PSD of the entire response of figure 7) computed using the KSE method with different sensor configurations.

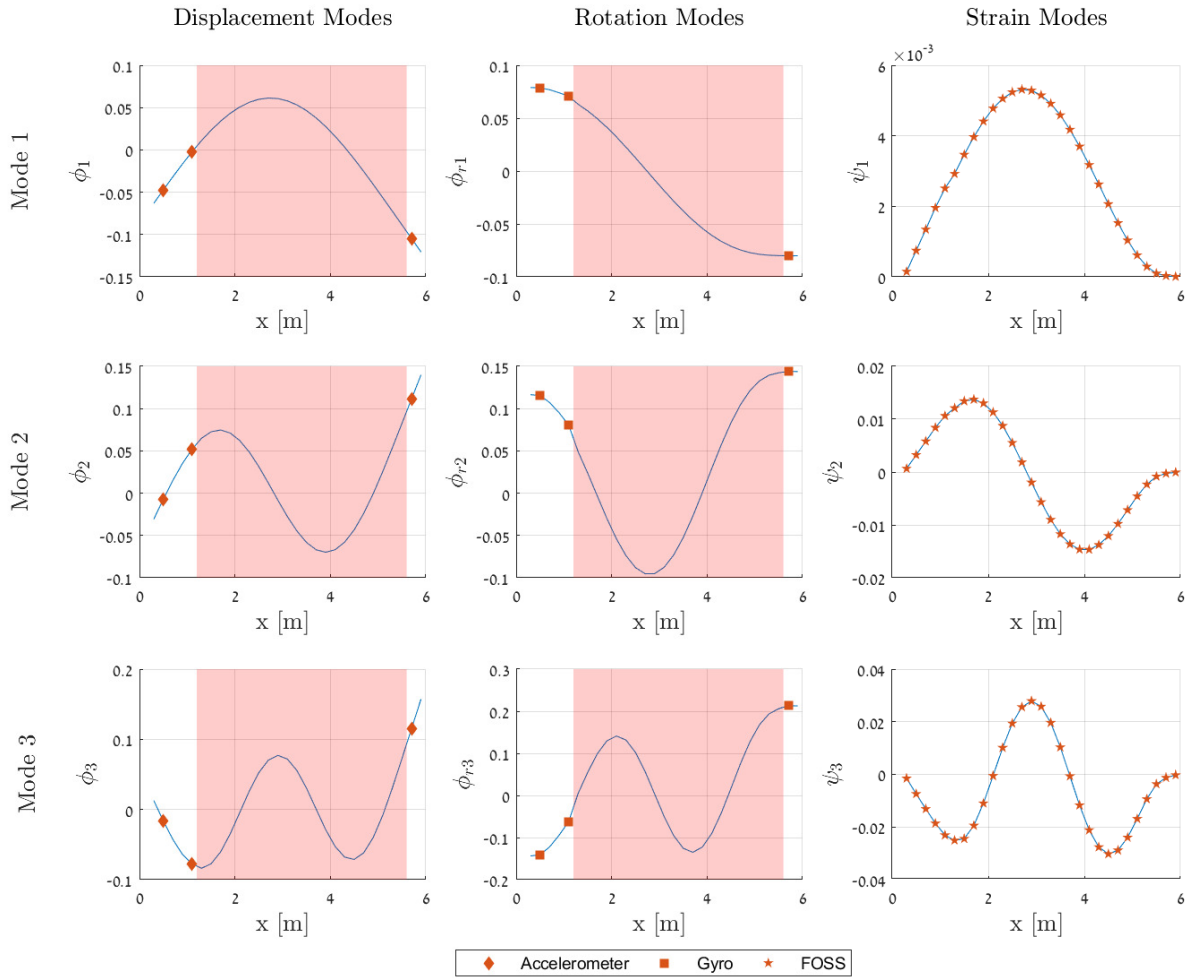


Figure 5: Different sensor locations along the missile structure shown over the first three elastic modes. The red-shaded area represents the rocket motor where accelerometers and gyros cannot be installed.

For all cases, the method successfully cleaned the elastic response component of all considered modes, leaving only the rigid body response at the vehicle's IMU location.

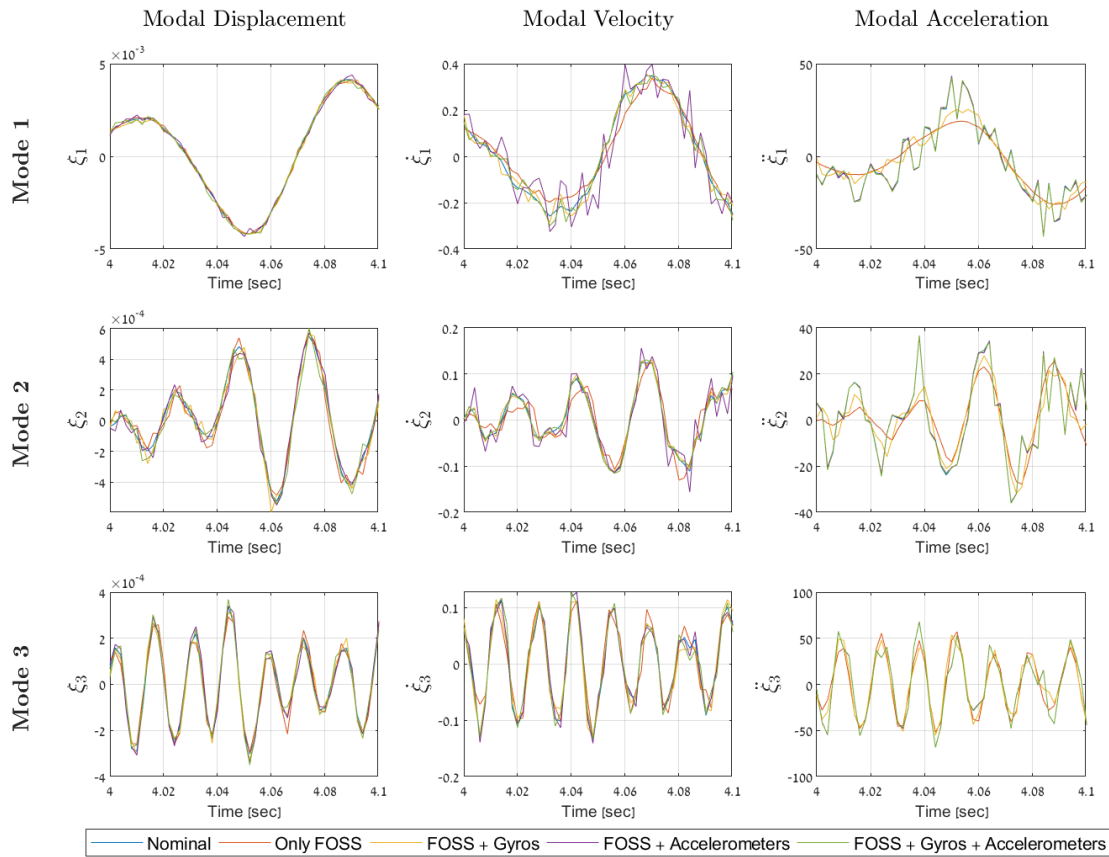


Figure 6: Comparison of the first three elastic modes modal response estimation computed using different sensor combinations. The figure displays only part of the full response, at times  $4.0s < t < 4.1s$ , for improved clarity.

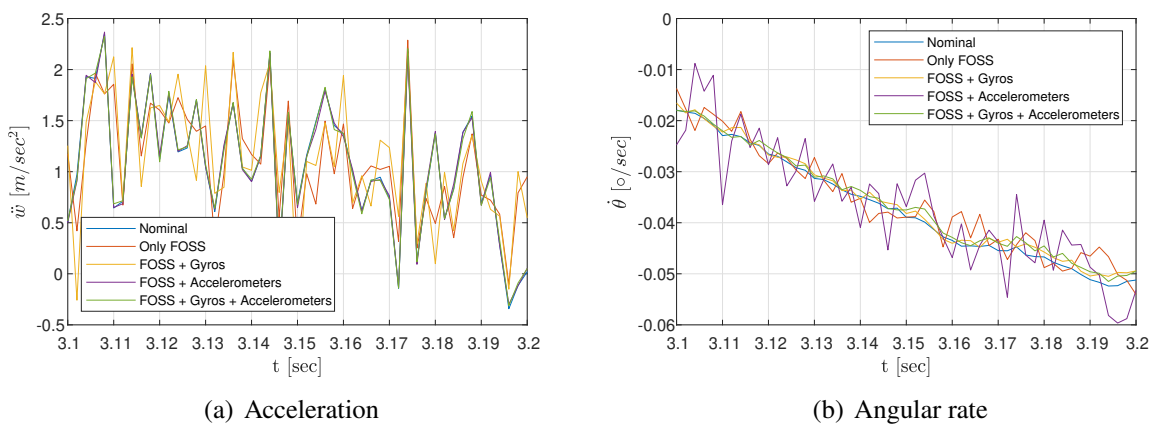


Figure 7: Computed rigid body (a) acceleration and (b) angular rate at the IMU location. The figure displays only part of the full response, at times  $3.1s < t < 3.2s$ , for improved clarity.

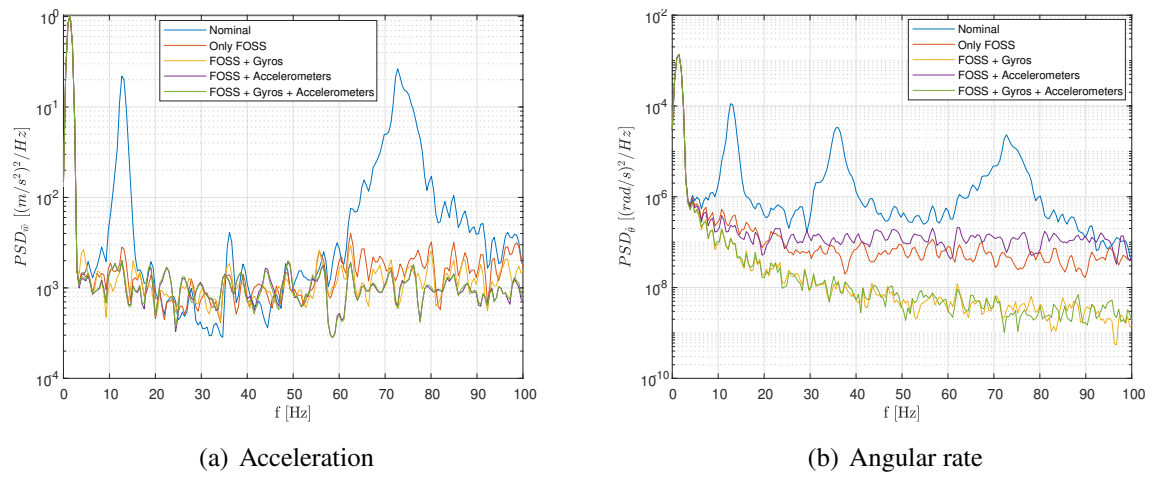


Figure 8: PSD of the rigid body (a) acceleration and (b) angular rate responses at the IMU location computed by the KSE using different sensor configurations.

### 4.3 Sensor noise level effect

Different sensors have different noise levels, whereby measurement noise may arise from electrical noise in the sensor's surrounding or inadequate signal conditioning. The Kalman gain is calculated using both process and measurement uncertainties, where based on their ratio, different weights are given for the prediction and the measurement. A high Q/R factor will result in an estimation mostly based on the measurements. If the measurement noise itself is high, the estimation will be noisy as well.

To investigate the effect of sensor noise levels, several noise levels were simulated for the case of estimation that uses a combination of FOSS, accelerometers, and gyros data. For each noise level, different sensor variance values were assigned to each sensor type. The variance values for the regular noise level were determined based on typical commercially available sensor datasheets, and the low and high noise variance levels were arbitrarily determined as a few orders of magnitude lower or higher than the regular value, to yield a significant difference in Q/R factor. Table 2 summarizes the sensor noise variance levels that were used.

Measurement	Strain $(\mu\text{S})^2$	Acceleration $\left(\frac{\text{m}}{\text{s}^2}\right)^2$	Angular Rate $\left(\frac{\text{rad}}{\text{s}}\right)^2$
Low Noise	0.1	$1 \times 10^{-5}$	$1 \times 10^{-8}$
Regular Noise	5	$1 \times 10^{-3}$	$5 \times 10^{-7}$
High Noise	1000	$5 \times 10^{-2}$	$1 \times 10^{-5}$

Table 2: Noise variance levels for each sensor type used to determine noise levels for sensitivity analysis.

Figure 9 shows the modal response estimation using the KSE for different levels of sensor noise. A close-up on a 0.1 sec representative section of the response is shown, such that the difference between different sensor configurations can be clearly seen.

Results in figure 9 show that for each modal response, the impact of noise levels is different. For the modal displacements, high noise value results in significantly noisy estimation, while for the modal velocities, the effect of noise is smaller and is mainly limited to the first mode. For the modal acceleration, the noise levels have a minor impact. These differences derive from the different noise levels of the different sensor types that are used to observe the modal displacements, velocities, and accelerations. Additionally, since the sensor noise is white Gaussian noise, its effect is more apparent in the first mode, where the responses are at a lower frequency relative to the measured frequency band, which contains noise at higher frequencies.

Figures 10 and 11 show the rigid body time response and PSD, respectively, at the IMU location computed by the KSE with different sensor noise levels. The results show that even for high sensor noise, the rigid body response is adequately computed, eliminating the elastic responses. In the case of high noise, the computed rigid body response is also noisy due to the broadband white noise, but the lower frequency physical response is well extracted.

### 4.4 Process noise level effect

The process noise in this study is bounded by some theoretical maximal response value for each of the states. The investigation uses different fractions of the maximal responses as a measure for different levels of process noise. The simulation was run using a combination of FOSS, accelerometers, and gyros, having regular sensor noise variance levels. In each simulation, a

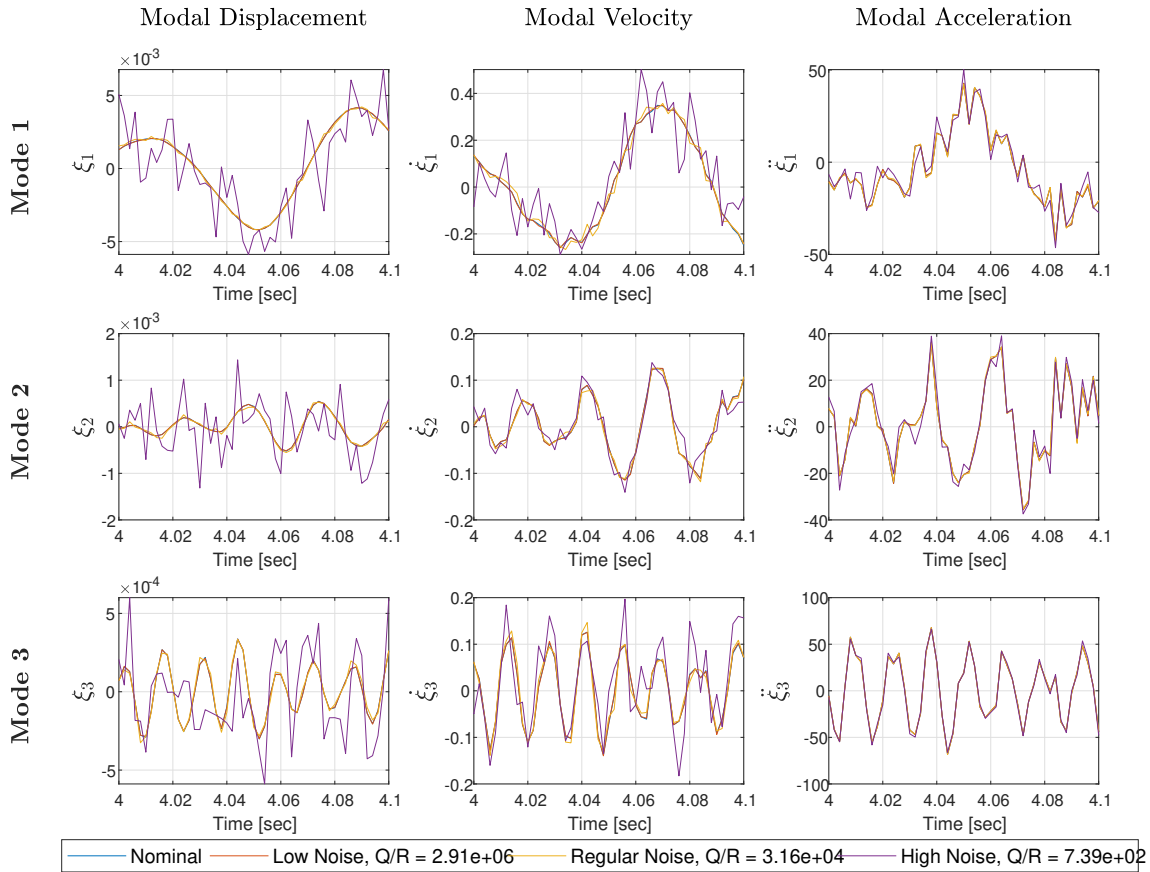


Figure 9: Comparison of the estimation of the modal responses of the first three elastic modes of the model, using different levels of sensors noise. The figure shows only part of the full response at times  $4 < t < 4.1$  for improved clarity. The calculated  $Q/R$  factor for each simulation is shown in the legend.

different fraction of the maximal modal response (36) was used, similar for all states. The process noise is directly proportional to the fraction value used, and the  $Q/R$  factor is proportional to its square value. The values used for sensitivity analysis were selected such that they yield various levels of  $Q/R$  factors that impact the KSE performance.

Figure 12 shows the RMS of the error between the nominal and the KSE-computed rigid body response as a function of the process noise, presented as a fraction of the maximal response value. The corresponding values of  $Q/R$  factor are also shown. At low process noise values (leading to a low  $Q/R$  factors), the process uncertainty is much lower than the measurement uncertainty, such that the KSE estimates the response mostly based on the model prediction. However, since the model is an approximate model, it fails to accurately predict the responses, hence the error in the rigid body response is large. At high fraction values (leading to a high  $Q/R$  factors), the estimation is based mostly on the measured data and thus converges to a constant RMS error for constant levels of sensor noise.

## 5 CONCLUSIONS

This study presented a method to estimate the elastic response of a slender body in flight using an approximate aeroelastic model and a combination of sensors utilizing the Kalman state estimator. The method was demonstrated on a test case of a simple slender body, showing the successful extraction of the rigid body response at the IMU location by subtracting the estimated elastic

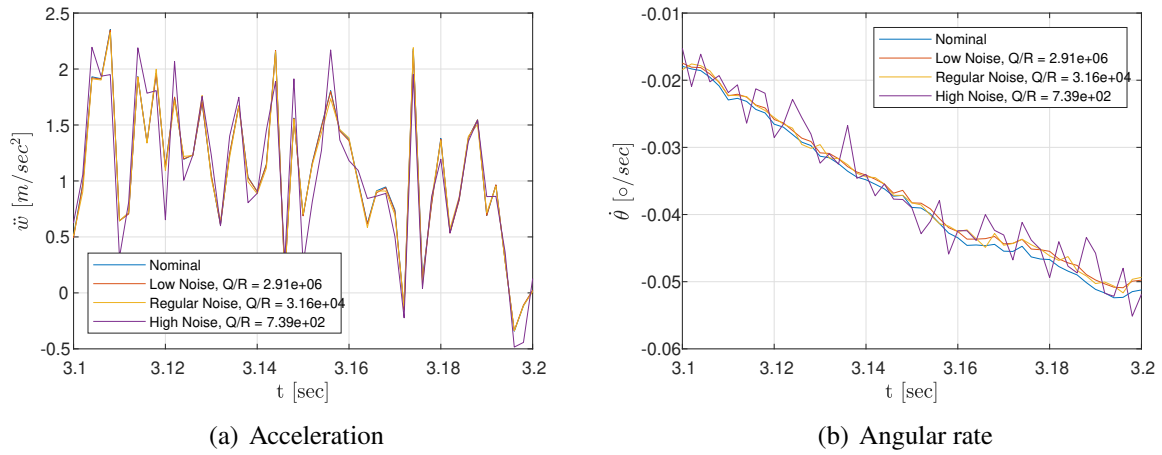


Figure 10: The rigid body response extraction of (a) acceleration and (b) angular rate for different noise levels. The figure shows only part of the full response at times  $3.1 < t < 3.2$  for improved clarity.

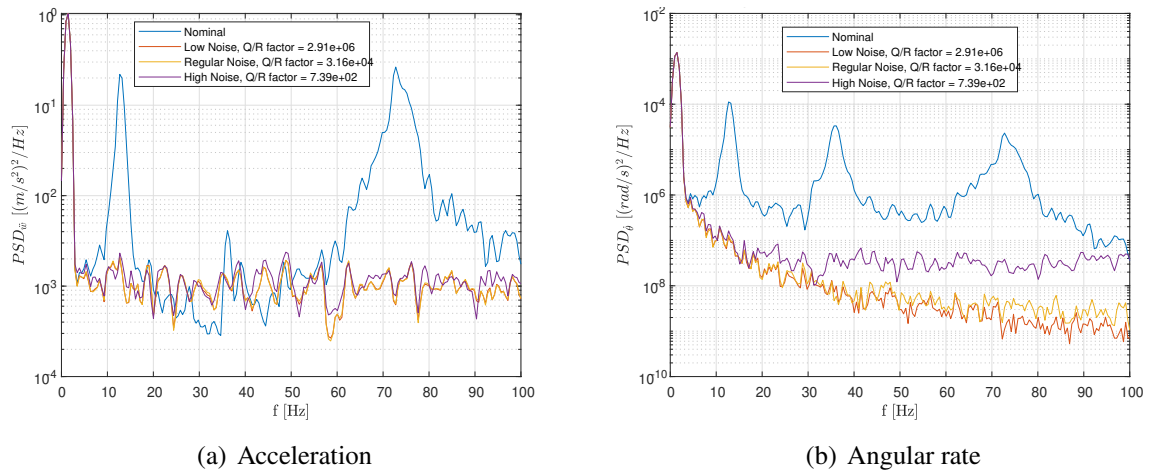


Figure 11: The PSD of the IMU extracted rigid body (a) acceleration and (b) angular rate responses for different noise levels. The PSD is calculated for the whole response.

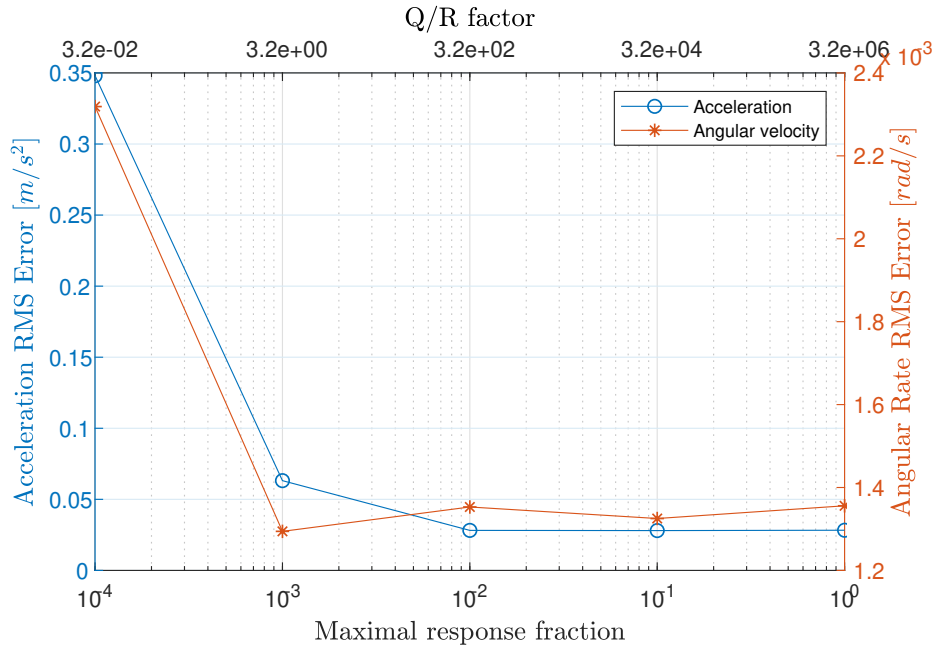


Figure 12: RMS error of the computed rigid body responses with varying process noise levels. The process noise is defined as the fraction of the maximal response for all states. The Q/R factor is calculated for each case.

response from the IMU measurements.

In order to estimate the elastic rates and accelerations, a modified aeroelastic formulation was presented, which includes the modal accelerations as states. With this formulation, all the considered measurements are directly proportional to a single state of the system, either modal displacement, velocity, or acceleration, through the corresponding normal modes set. This provided for improved estimation of the modal accelerations and the physical elastic acceleration response.

The test case results showed the feasibility of implementing the proposed approach on a real structure, considering practical constraints on sensor's installation. The results showed that using sensors whose measured data is proportional to some modal response, leads to the best estimation of that modal response, and the best reconstruction of physical responses calculated based on that modal response. In general, as expected, having all types of sensors at measurement points, such that all modes are observable and differentiable, yields the best estimation of all parameters. However, even in cases in which there is no sensor proportional to some of the modal responses, adequate estimation of all the modal responses is achieved, leading to adequate reconstruction of the elastic response at unmeasured points and the elimination of the elastic response from the overall measurement at the IMU point.

Finally, the effect of measurement and process uncertainties were analysed using some bounding values without full tuning of the uncertainty matrices. The analysis showed that using an approximated model increases the process noise (that compensates for the approximation), and leads to an estimation that is mostly based on the measured data. However, even in cases of noisy sensors, which yield a noisy estimation, an adequate reconstruction of the elastic response, and consequently, elimination of the elastic response from the overall measured data is attainable.

## 6 REFERENCES

- [1] Noll, R. B. and Zvara, J. (1971). Structural interaction with control systems. Tech. Rep. 8079, NASA.
- [2] Choi, H. D. and Kim, J. (2001). Adaptive notch filter design for bending vibration of a sounding rocket. *Proceedings of the Institution of Mechanical Engineers, Part G: Journal of Aerospace Engineering*, 215(1), 13–23. doi:10.1243/0954410011531718.
- [3] Joels, T. and Raveh, D. E. (2023). Wing dynamic shape-sensing from fiber-optic strain data using the kalman state estimator. *Aerospace Science and Technology*, 137, 108286. ISSN 1270-9638. doi:<https://doi.org/10.1016/j.ast.2023.108286>.
- [4] Karpel, M. (1982). Design for active flutter suppression and gust alleviation using state-space aeroelastic modeling. *Journal of Aircraft*, 19(3), 221–227.
- [5] Technology, Z. (2017). *ZAERO Version 9.32 THEORETICAL MANUAL*. ZONA Technology Inc., Scottsdale, AZ, 4th ed. Available at <https://www.zonatech.com/downloads.html>.
- [6] Kalman, R. E. (1960). A new approach to linear filtering and prediction problems. *Journal of Basic Engineering*, 82(1), 35–45.
- [7] Roger, K. L. (1977). Airplane math modeling methods for active control design.
- [8] Karpel, M. (1981). Design for active and passive flutter suppression and gust alleviation. Tech. Rep. 3482, NASA.
- [9] Irvine, T. (2011). Prediction of sound pressure levels on rocket vehicles during ascent. *Revision E, Vibrationdata*.

## COPYRIGHT STATEMENT

The authors confirm that they, and/or their company or organization, hold copyright on all of the original material included in this paper. The authors also confirm that they have obtained permission from the copyright holder of any third-party material included in this paper to publish it as part of their paper. The authors confirm that they give permission, or have obtained permission from the copyright holder of this paper, for the publication and public distribution of this paper as part of the IFASD 2024 proceedings or as individual off-prints from the proceedings.